Identifying the Optimum Morphology in High-Performance Perovskite Solar Cells

Guijun Li, Kwong Lung Ching, Jacob Y. L. Ho, Man Wong, and Hoi-Sing Kwok**

Advances in photovoltaics (PV) technologies assure to expedite the large-scale implementation, which requires either significantly higher energy conversion efficiencies or exceedingly lower fabrication costs. Although the mainstream silicon-based solar cell technology is considered as a long-term player and has dominated the PV market over the last 30 years; opportunities still exist for technologies that offer innovative concepts and advanced materials.[1–3] A recent rapid emergence of a newcomer in the PV field is the hybrid organic–inorganic halide perovskite solar cell, the conversion efficiency of which has advanced from 3.8% reported in 2009 to a confirmed extremely high efficiency of 17.9% in the early 2014,[4,5] due to fantastic features such as their high absorption coefficient, low nonradiative carrier recombination rate, and long-range balanced carrier transport length.[5–7] Furthermore, such organic–inorganic systems can be prepared and fabricated from an inexpensively low temperature solution process,[8] thereby creating the opportunity for cost-effective manufacture and offering the potential for physical flexibility.[9]

Critical to the solution process is the morphology of the perovskite active layer, since the perovskite crystal formation largely depends on the interfacial energy, solution concentration, precursor composition, solvent choice, and deposition temperature.[9–13] Most recently, efforts have been done to increase the surface coverage by varying processing conditions,[12–14] incorporating additives,[15] and using the mixed solvent of γ-butyrolactone and dimethylsulphoxide followed by toluene drop-casting.[11] Despite the resulting improvement of the cell efficiency, where a high surface coverage is no longer an issue, still large deviations for efficiency are observed due to nonuniform film thickness. Besides the poor film uniformity, issues also arise from little understanding of the same fundamental properties of the perovskite, which is especially true for the device structure. Indeed, the device structure evolution that develops from the mesoscopic to the planar architectures increases the diversity of approaches that gave reasonable performances. Ongoing improvement in the performance of the device requires identifying the optimum morphology with a reliable structure to achieve high-performance solar cells.

G. Li, K. L. Ching, J. Y. L. Ho, Prof. M. Wong, Prof. H.-S. Kwok
State Key Laboratory on Advanced Displays and Optoelectronics Technologies
Department of Electronic and Computer Engineering
Hong Kong University of Science and Technology
Clear Water Bay
Kowloon, Hong Kong
E-mail: gliad@connect.ust.hk; eekwok@ust.hk

DOI: 10.1002/aenm.201401775

Perovskite-sensitized solar cell with a record power-conversion efficiency (PCE) of 15% was reported using a sequential deposition process.[16] This method allows much better control over the perovskite morphology within the nanoporous host and so consequently it is of great interest. However, the V_{oc} obtained is generally lower than 1 V, limiting the further boost of the efficiency. In fact, V_{oc} up to 1.1 V could be practically obtained by using an Al_2O_3 scaffold to replace the TiO_2 mesoporous structure. Here, we investigate the morphology of the perovskite active layer. We provide a variety of controllable perovskite morphologies by employing different fabrication approaches conducted in the ambient atmosphere. We correlate the morphology to the solar cell performance. A bilayer structure, which has a combination of the strengths of the mesoscopic and planar structure is identified to be essential for realizing high-performance perovskite solar cells with high reproducibility.

Figure 1 presents the scanning electron microscopy (SEM) images of the PbI_2 and the resultant $CH_3NH_3PbI_3$ films, fabricated on the FTO/mp-TiO_2. The PbI_2, which is deposited on the substrate by spin coating from the *N,N*-dimethylformamide (DMF) solution, will infiltrate into the nanopores of the mp-TiO_2 network. In addition, a typical continuous capping layer of thickness 100–150 nm will be conformably formed on the top due to the excessive solvent. This capping layer is composed of platelet-shaped PbI_2 crystals that are between 50 and 150 nm in diameter and fully covers the mp-TiO_2 surface, as shown in Figure 1a. Once the PbI_2 film is brought into contact with the CH_3NH_3I solution, the conversion of the PbI_2 into the 3D perovskite, $CH_3NH_3PbI_3$ is facilitated through the insertion of the CH_3NH_3I into the layered-PbI_2 framework. Figure 1b is the representative $CH_3NH_3PbI_3$ morphology after the dipping of the PbI_2 film in a solution of the CH_3NH_3I (10 mg mL^{-1} in 2-proponal). The consumption of the PbI_2 and the expansion of the interlayer distance along the *c*-axis during the crystal growth result in a more porous and high surface roughness $CH_3NH_3PbI_3$ upper layer, which is composed of a great number of tetragonal-shaped discrete crystals that are randomly distributed and poorly interconnected. The grain size of the $CH_3NH_3PbI_3$ in the mesoporous host is limited by the pore size of the mp-TiO_2, while the dimensions of the $CH_3NH_3PbI_3$ crystals on the top surface vary between 50 and 200 nm. The crystal formation process, which is relatively unconstrained in the 2-proponal, is responsible for forming the film characterized with much porosity and a high surface roughness. Correspondingly, the exposure of the mp-TiO_2 is unavoidable. As illuminated in **Figure 2**a, the feature of this morphology is such that some of the hole-transporting material (HTM) comes in contact with the $CH_3NH_3PbI_3$ in a nanoscale domain, as is

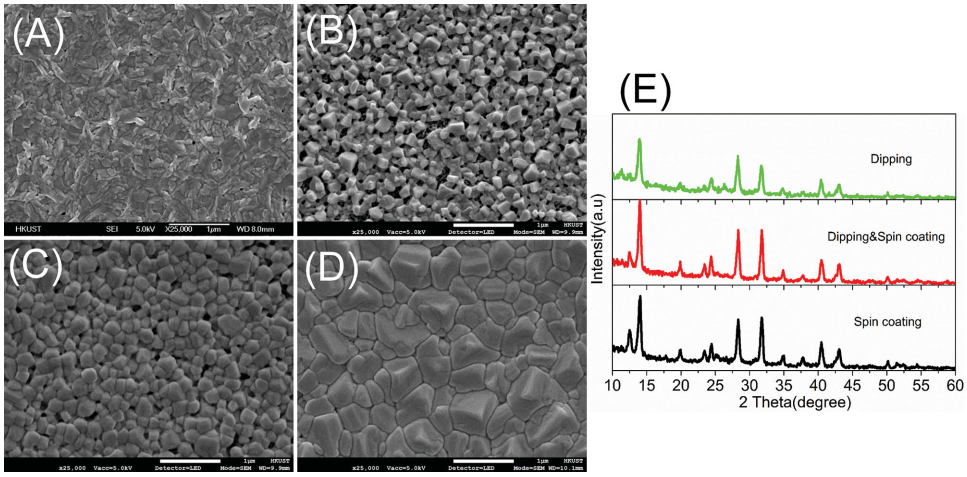

Figure 1. The top-view SEM images of a) PbI_2 film fabricated from the spin coating of the DMF solution; b) $CH_3NH_3PbI_3$ film fabricated from the immersion of the PbI_2 in the CH_3NH_3I/2-proponal solution (10 mg mL^{-1}); c) $CH_3NH_3PbI_3$ film fabricated from the spin coating of the PbI_2 from the CH_3NH_3I/2-proponal solution (30 mg mL^{-1}); d) $CH_3NH_3PbI_3$ film fabricated from the immersion of the PbI_2 in the CH_3NH_3I/2-proponal solution (8.5 mg mL^{-1}), followed by the spin coating of the as fabricated film from the CH_3NH_3I/2-proponal solution (20 mg mL^{-1}). e) X-ray diffraction spectra of mesoporous TiO_2 films infiltrated with different $CH_3NH_3PbI_3$ films with different morphologies fabricated from different formation processes. The peak at 12.56° is related to the PbI_2.

the case for the mesoscopic solar cell, by penetrating into the mesoporous structure through the porous upper layer. The evidence of the infiltration of the HTM into the mesoporous scaffold was reported earlier.[17] In order to closely interconnect the discrete $CH_3NH_3PbI_3$ crystals, external factors should be applied during the crystal formation. The spin coating of the CH_3NH_3I (30 mg mL^{-1}), instead of the immersion process, is used to densify the $CH_3NH_3PbI_3$ upper layer. In this way, the upper layer morphology transitions from a continuous PbI_2 layer into a continuous $CH_3NH_3PbI_3$ layer, composed of well-connected perovskite crystals ranging from 50 to 200 nm is shown in Figure 1c. The spreading flow due to the centrifugal force during the spin coating plays a substantial role in driving the discrete $CH_3NH_3PbI_3$ crystals to be sufficiently connected. However, the complete conversion of the PbI_2 to the $CH_3NH_3PbI_3$ is hindered, which is observed from the XRD measurement (Figure 1e). To completely transform the PbI_2 into the $CH_3NH_3PbI_3$ and further densify the perovskite upper layer, the following procedure is proposed: the PbI_2 film is first immersed in the CH_3NH_3I solution with a concentration of 8.5 mg mL^{-1}, followed by the spin coating of a 20 mg mL^{-1} CH_3NH_3I solution. The film fabricated from this two-steps process still shows obvious PbI_2 peak at 12.56°, with intensity smaller than that of the film obtained from the spin coating process. Because the film from dipping process has no obvious peak of PbI_2, the appearance of the PbI_2 is probably due to degradation of the perovskite film during the spin coating, which is conducted in the ambient atmosphere without controlling the moisture. For the spin-coated film, complete conversion of the PbI2 to the CH3NH3PbI3 is hindered, because the nucleation and growth of the perovskite is terminated due to the formation of a relatively continuous capping layer on the surface and the perovskite film is dissolved by the moisture during the spin coating process. The resulting morphology of the two-steps film is shown in Figure 1d. The immersion process produces the large crystals and the spin coating process densifies the large crystals and fills the gaps with small crystals (these small crystals are formed during the spin coating process). In addition, from the cross-sectional SEM image (**Figure 3**a), the perovskite formed in the mp-TiO_2, as is the case

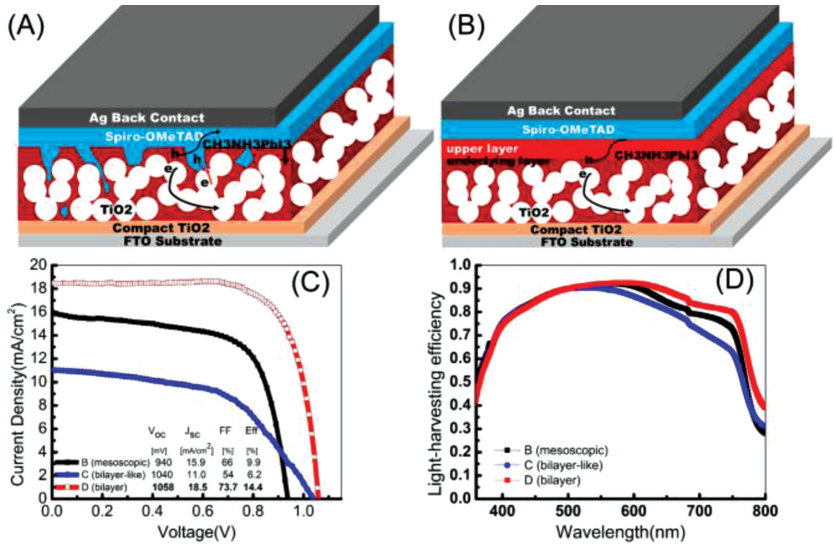

Figure 2. The schematic of the perovskite solar cells with a) a mesoporous structure; b) a bilayer structure. c) The *J*–*V* curves of the perovskite solar cells with different morphologies; d) light harvesting efficiency of the perovskite solar cells with different morphologies. The B (mesoscopic), C (bilayer-like), and D (bilayer) are corresponding to the morphologies shown in Figure 1b–d, respectively.

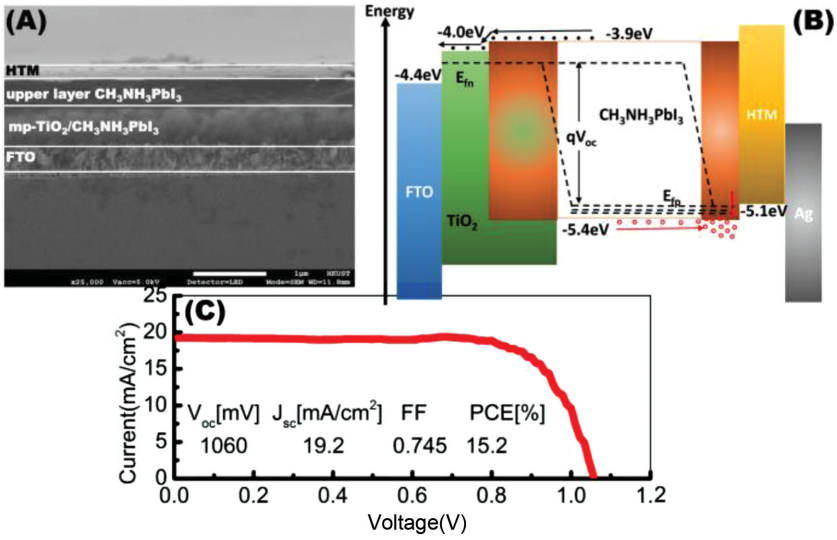

Figure 3. a) Cross-sectional SEM image of a bilayer perovskite device; b) illumination of quasi-Fermi level down shift in an energy band diagram of the bilayer structure. c) Current–voltage curve of the best performance perovskite solar cell with a bilayer structure.

in the Figure 1b,c is characterized by the mesoporous structure; on the contrary, the upper perovskite layer is extremely compact and has 100% surface coverage. Consequently, the interface between the perovskite and HTM is more like the "planar-heterojunction", which, along with the "distributed junction" of the interface between the mp-TiO_2 and perovskite, forms a bilayer structure, as illuminated in Figure 2b. For the device with the morphology shown in Figure 1c, although full surface coverage is obtained, it is not totally compact and hereafter regarded as a "bilayer-like" structure.

In order to elucidate the relation between the morphology and the photovoltaic performance, devices are fabricated and the current–voltage (J–V) characteristics are measured under simulated standard AM1.5G illumination (100 mW cm^{-2}). The J–V curve of a typical device based on the "mesoscopic" structure (Figure 1b) is shown as the black trace in Figure 2c, from which the J_{sc}, V_{oc}, FF, and PCE are determined to be 15.9 mA cm^{-2}, 940 mV, 66%, and 9.9%, respectively. A typical device based on the "bilayer-like" structure (Figure 1c) is shown as the blue trace, with PCE = 6.2%, J_{sc} = 11 mA cm^{-2}, V_{oc} = 1040 mV, and FF = 54%. Significant improvement of the V_{oc} is observed but the rising series resistance calculated from the J–V curve slope at the open-circuit condition gives rise to the lower FF, probably arising from the unreacted PbI_2. Meanwhile, the J_{sc} is also found decreased, suggesting insufficient light absorption and inefficient carrier collection. As expected, the solar cell based on the bilayer morphology (Figure 1d) shows a J_{sc} of 18.5 mA cm^{-2}, V_{oc} of 1058 mV, and FF of 73.7%; the conversion efficiency is successfully increased up to 14.4%. The highest-performing device based on the bilayer structure achieves a conversion efficiency of 15.2%, with J_{sc}, V_{oc}, and FF of 19.2 mA cm^{-2}, 1060 mV, and 74.5% respectively. The J–V curve of the best cell is shown in Figure 3c. The results above clearly suggest that the bilayer structure has a distinct advantage over the mesoporous structure—its V_{oc} is about 100–150 mV greater than that of the solar cell with the mesoporous structure, combined with the pronounced improvement of the J_{sc} and FF, leading to a remarkable high efficiency solar cell.

It is worth noting that a relatively high concentration of the CH_3NH_3I is used for the spin coating process. **Table 1** depicts the photovoltaic parameters of the devices prepared by using the different concentrations of the CH_3NH_3I. The cell with 40 mg mL^{-1} shows a high V_{oc} of up to 1110 mV. Lowering the concentration will slightly decrease the V_{oc}, accompanied by an increase in the photocurrent. The concentration of the CH3NH3I has a large impact on the grain size of the perovskite. The lower the concentration, the larger the grain size.[18] A large grain size will favor the photocurrent due to the light scattering. The optimized concentration is 20–30 mg mL^{-1}, where the highest FF is obtained. The impressively high V_{oc}, which was previously demonstrated by using the dielectric Al_2O_3 scaffold system with the ability to exhibit exceptionally few fundamental energy losses[19] can also be obtained by using the anatase mp-TiO_2 system in our case only by using a bilayer structure even without judicious selection of the perovskite lead halide-based absorber or control over band offsets.[20–22] Another recent study that used a rutile nanoparticle TiO_2 reached a similar result (1110 mV) with a planar heterojunction structure;[23] we thus can postulate that the planar-heterojunction (the interface between the HTM and perovskite) in the bilayer structure plays a role in the enhancement of the V_{oc}, which will be discussed later.

To shed light on the role of the morphology in the light absorption, the light-harvesting efficiency of the perovskite absorber is measured according to the methodology of Snaith and co-workers.[8] The results are shown in Figure 2d. The light-harvesting efficiencies at the short wavelength range (<550 nm) are almost the same for different morphologies, since most of the light within the spectrum can be totally absorbed by the underlying perovskite layers that are almost identical in all cases. The difference among the light absorption at the long wavelength arises mainly from the different morphologies of the upper layers, for example, the roughness, the surface coverage, and the density of the absorbing materials. In principle, a full surface coverage and high surface roughness active layer can give rise to more light absorption.[14,24] The unexpected decrease of the light absorption in the "bilayer-like" device (Figure 1c) is

Table 1. Characteristics of the cells with different CH3NH3I concentration used during spin coating.

CH_3NH_3I in 2-proponal	V_{oc} [mV]	J_{sc} [mA cm^{-2}]	FF [%]	PCE [%]
15 mg mL^{-1}	1032	18.8	65	12.6
20 mg mL^{-1}	1058	18.5	73.7	14.4
30 mg mL^{-1}	1060	18.3	72.3	14
40 mg mL^{-1}	1100	16.4	59	10.7

partly attributed to the incomplete transformation of the PbI_2 into the $CH_3NH_3PbI_3$, which could clearly be observed from the color of the sample. However, this effect on the light absorption of the "bilayer structure" device is thought to be insignificant due to the small amount of the PbI_2 formed during the spin coating. Additionally, the device with a bilayer structure (Figure 1d) has higher absorption than that of the device with a mesoporous structure (Figure 1b) due to the high density active material and 100% full surface coverage. However, the difference in the light-harvesting efficiency between the bilayer and the mesoporous structures does not account for the difference in the photocurrent shown in Figure 2c, it is believed that the recombination loss also contributes to the difference of the J_{sc}.

We now discuss the V_{oc} case. Apparently, the perovskite upper layer plays a key role to determine the device performance. The origin of the V_{oc} improvement could be easily directed to a more compact and uniform upper layer. In the mesoporous structure shown in Figure 2a, it is possible for the HTM to be directly contacted with the exposed mp-TiO_2 so that the recombination between electrons in the TiO_2 conduction band and holes in the HTM is unavoidable. The 100% full surface coverage of the mp-TiO_2 with perovskite crystals densely interconnected can effectively help avoid the undesired recombination, which represents one of the major problems that deteriorates the device performance by increasing the shunt saturation current and reducing the photogenerated charge carriers. To some extent, this situation is further manifested by totally removing the upper layer in the case of a thick mp-TiO_2, for instance, 600 nm, so that the V_{oc} suffers from a considerable decrease due to the dramatical increase in the recombination rate. In addition, the surface roughness is expected to have an effect on the V_{oc}. We perform AFM analysis of different morphologies as shown in **Figure 4**. The root mean squares (RMS) are determined to be 21, 40, 26, and 22 nm for the PbI_2 film, and $CH_3NH_3PbI_3$ films shown in Figure 1b–d, respectively. The smaller the RMS of the upper layer, the higher the V_{oc}. The same tendency is also true and widely reported in other types of solar cells. For example, in the silicon-based thin film solar cell, the V_{oc} suffers from a pronounced loss when a highly texturing substrate is used, due to the increased local creation of defective material such as cracks or porosity.[24] In our case, the high RMS of the perovskite upper layer will increase the possibility of short-circuiting the device existing between the silver electrode and the perovskite absorber, in the case that the HTM cannot fully cover the perovskite film. In other words, a high roughness perovskite upper layer requires a thick HTM in order to eliminate the short-circuiting. On the contrary, a thin HTM layer is preferred to assure a reasonable FF due to the low conductivity of the spiro-MeOTAD.

From the direct and inverse photoemission spectroscopy studies, the V_{oc} obtained for the $CH_3NH_3PbI_3$ mesoscopic solar cell should be equal to 1.0 V.[25] However, the V_{oc} obtained in our device is 1.11 V, indicating that there are other mechanisms, beyond the reduced recombination rate discussed above. As we know, the V_{oc} is determined by the potential

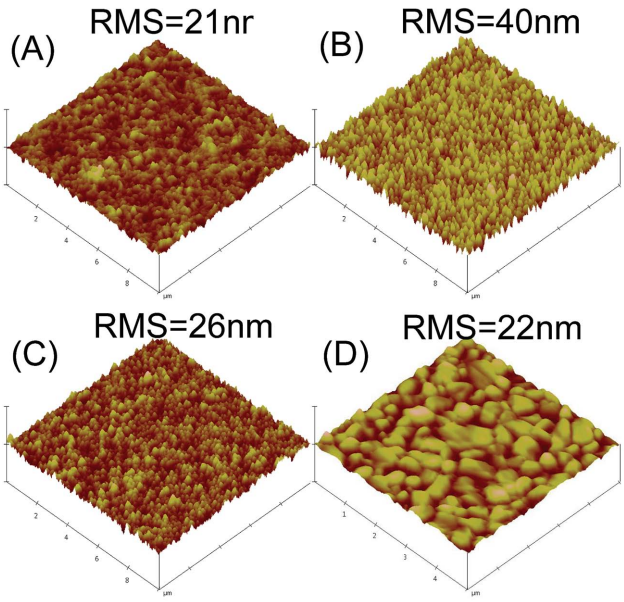

Figure 4. The atomic force microscopy (AFM) images of a) PbI_2 film; b) $CH_3NH_3PbI_3$ film shown in Figure 1b; c) $CH_3NH_3PbI_3$ film shown in Figure 1c; d) $CH_3NH_3PbI_3$ film shown in Figure 1d. The scale bar in *z*-direction is 500 nm div^{-1}.

difference between the quasi-Fermi level of the electron (E_{fn}) in the n-type material and the quasi-Fermi level of the hole (E_{fp}) in the p-type material under illumination.[19] The splitting of the quasi-Fermi level is thus believed to play a critical role in improving the V_{oc} up to 1110 mV. This is illuminated in Figure 3b. On the side of the mp-TiO_2/perovskite, it is similar to the sensitized solar cell that the quasi-Fermi level is determined by the mp-TiO_2, since the underlayer is mesoporous structured, electrons will quickly inject into the mp-TiO_2. However, on the side of perovskite/HTM with a planar heterojunction, the photogenerated holes have to transport to the HTM, and they will accumulate in the perovskite upper layer, due to the high capacitance of the perovskite material.[26] The unexpected accumulation of the hole will downshift the quasi-Fermi level to the valence band of $CH_3NH_3PbI_3$. The downshift of the E_{fp} increases the potential difference, and thereby improves the

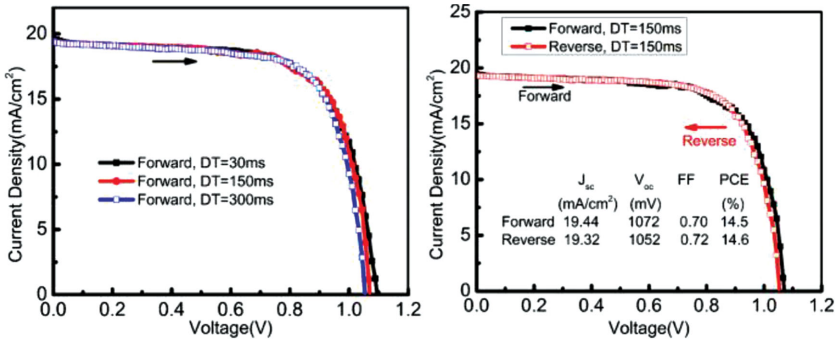

Figure 5. Current density–voltage curves of the bilayer structure perovskite solar cell with a) different dwell time; b) scan directions. Dwell time is the time required to measure the current at a given voltage. Reverse scan defines a measure from the open-circuit to the short-circuit and forward scan is vice-versa.

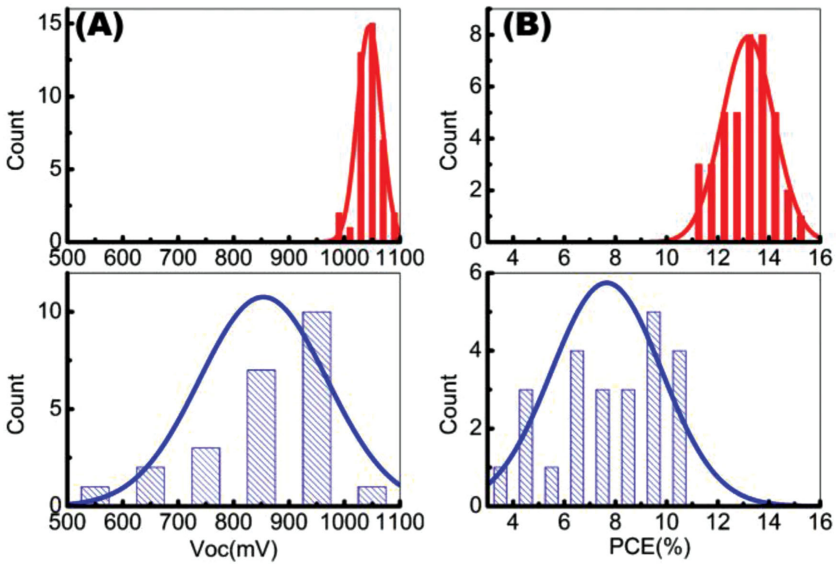

Figure 6. Histograms of the cell-performance characteristics a) V_{oc}; b) PCE. The red bars is the results of the devices with a bilayer structure, the blue bars is the results of the devices with a mesoporous structure.

V_{oc}. Furthermore, in the sensitized solar cell with a mesoporous structure, the electrons and holes injection process is accompanied by the fundamental energy loss. However, for the devices with a continuous upper perovskite layer in a bilayer structure, the exciton binding energy is still sufficiently low for thermal dissociation of excitons into free carriers, the charge transfer energy loss can be avoided, and as a result, the voltage output is also expected to be high.

The anomalous hysteresis was shown to be a major issue in evaluating the perovskite solar cell. In order to accurately characterize the cell efficiency, we measured the "bilayer structure" high-efficiency device by changing the scanning directions and the dwell time, which referred to the time required to measure the current at a given voltage. *J*–*V* results are shown in **Figure 5**. The *J*–*V* of the forward and reverse scans are well coincident, while varying the dwell time can induce a considerable error of the cell efficiency. However, the deviation is so small that the cell efficiency decreases from 14.7% to 14.4% when the dwell time increases from 30 to 300 ms.

To investigate the reproducibility of the results, 24 cells with the mesoporous structure and 40 cells with the bilayer structure are fabricated. Histograms of the cell-performance characteristics are shown in **Figure 6**. It is clearly shown that the devices with mesoporous structure have very large V_{oc} and efficiency fluctuations, which relates to the morphology variation even that the fabrication is conducted carefully to make sure the processes are kept the same at all times. On the contrary, the reproducibility of the devices with the bilayer structure performs extremely well, more than 95% of the devices have the V_{oc} in excess of 1.0 V, and 80% of the devices have the efficiency larger than 12%. The relatively large deviations of the PCE compared with the V_{oc} mainly comes from the FF, which may result from the variation in the thickness of the HTM. The extremely small derivation of V_{oc} indicates the perovskite upper has a large area of uniformity and a reliable repeatable morphology.

In summary, we presented a variety of controllable morphologies for the perovskite solar cells, and identified how the morphology of the perovskite absorbing layer affects the performance of perovskite solar cells. Consequently, we show that a bilayer structure, which is composed of a compact upper layer and a mesoporous structured underlayer, has a distinct advantage over the mesoporous structure not only in the conversion efficiency, but also in the reproducibility. Our comparative study of the bilayer and mesoporous structures tells us about the optimum morphology that is required for efficient solar cells, of which we demonstrate with high efficiencies of up to 15.2% and V_{oc} of up to 1110 mV. The origin of the improvement V_{oc} is attributed to the suppressing of the recombination as well as the shift of the quasi-Fermi level. Furthermore, the 80% high yield also paves the way for the possibility of mass production in the future, even though the fabrication process is conducted in the ambient atmosphere without controlling moisture.

Supporting Information

Supporting Information is available from the Wiley Online Library or from the author.

Acknowledgements

This work was funded by the Partner State Key Laboratory on Advanced Displays and Optoelectronics Technologies (PSKL).

Received: October 8, 2014
Revised: November 15, 2014
Published online: January 29, 2015

[1] M. L. Brongersma, Y. Cui, S. Fan, *Nat. Mater.* **2014**, *13*, 451.
[2] G. Li, J. Y. L. Ho, H. Li, H.-S. Kwok, *Appl. Phys. Lett.* **2014**, *104*, 231113.
[3] J. D. Major, R. E. Treharne, L. J. Phillips, K. Durose, *Nature* **2014**, *511*, 334.
[4] A. Kojima, K. Teshima, Y. Shirai, T. Miyasaka, *J. Am. Chem. Soc.* **2009**, *131*, 6050.
[5] M. A. Green, A. Ho-Baillie, H. J. Snaith, *Nat. Photonics* **2014**, *8*, 506.
[6] H. J. Snaith, *J. Phys. Chem. Lett.* **2013**, *4*, 3623.
[7] S. D. Stranks, G. E. Eperon, G. Grancini, C. Menelaou, M. J. P. Alcocer, T. Leijtens, L. M. Herz, A. Petrozza, H. J. Snaith, *Science* **2013**, *342*, 341.
[8] J. M. Ball, M. M. Lee, A. Hey, H. J. Snaith, *Energy Environ. Sci.* **2013**, *6*, 1739.
[9] P. Docampo, J. M. Ball, M. Darwich, G. E. Eperon, H. J. Snaith, *Nat. Commun.* **2013**, *4*, 2761.

[10] B. Conings, L. Baeten, C. De Dobbelaere, J. D'Haen, J. Manca, H.-G. Boyen, *Adv. Mater.* **2014**, *26*, 2041.
[11] N. J. Jeon, J. H. Noh, Y. C. Kim, W. S. Yang, S. Ryu, S. I. Seok, *Nat. Mater.* **2014**,*13*, 897.
[12] A. Dualeh, N. Tétreault, T. Moehl, P. Gao, M. K. Nazeeruddin, M. Grätzel, *Adv. Funct. Mater.* **2014**, *24*, 3250.
[13] M. Saliba, K. W. Tan, H. Sai, D. T. Moore, T. Scott, W. Zhang, L. A. Estroff, U. Wiesner, H. J. Snaith, *J. Phys. Chem. C* **2014**, *118*,17171.
[14] G. E. Eperon, V. M. Burlakov, P. Docampo, A. Goriely, H. J. Snaith, *Adv. Funct. Mater.* **2014**, *24*, 151.
[15] P.-W. Liang, C.-Y. Liao, C.-C. Chueh, F. Zuo, S. T. Williams, X.-K. Xin, J. Lin, A. K. -Y. Jen, *Adv. Mater.* **2014**, *26*, 3748.
[16] J. Burschka, N. Pellet, S.-J. Moon, R. Humphry-Baker, P. Gao, M. K. Nazeeruddin, M. Grätzel, *Nature* **2013**, *499*, 316.
[17] D. Nanova, A. K. Kast, M. Pfannmöller, C. Müller, L. Veith, I. Wacker, M. Agari, W. Hermes, P. Erk, W. Kowalsky, R. R. Schröder, R. Lovrinčić, *Nano Lett.* **2014**, *14*, 2735.
[18] J.-H. Im, I.-H. Jang, N. Pellet, M. Grätzel, N.-G. Park, *Nat. Nanotechnol.* **2014**, *9*, 927.
[19] M. M. Lee, J. Teuscher, T. Miyasaka, T. N. Murakami, H. J. Snaith, *Science* **2012**, *338*, 643.
[20] E. Edri, S. Kirmayer, M. Kulbak, G. Hodes, D. Cahen, *J. Phys. Chem. Lett.* **2014**, *5*, 429.
[21] E. Edri, S. Kirmayer, D. Cahen, G. Hodes, *J. Phys. Chem. Lett.* **2013**, *4*, 897.
[22] S. Ryu, J. H. Noh, N. J. Jeon, Y. Chan Kim, W. S. Yang, J. Seo, S. I. Seok, *Energy Environ. Sci.* **2014**, *7*, 2614.
[23] A. Yella, L.-P. Heiniger, P. Gao, M. K. Nazeeruddin, M. Grätzel, *Nano Lett.* **2014**, *14*, 2591.
[24] G. Li, H. Li, J. Y. L. Ho, M. Wong, H. S. Kwok, *Nano Lett.* **2014**, *14*, 2563.
[25] P. Schulz, E. Edri, S. Kirmayer, G. Hodes, D. Cahen, A. Kahn, *Energy Environ. Sci.* **2014**, *7*, 1377.
[26] H.-S. Kim, I. Mora-Sero, V. Gonzalez-Pedro, F. Fabregat-Santiago, E. J. Juarez-Perez, N.-G. Park, J. Bisquert, *Nat. Commun.* **2013**, *4*, 2242.